Three-dimensional wind-turbine wake characterization via tomographic particle-image velocimetry

Three-dimensional wind-turbine wake characterization via tomographic particle-image velocimetry

Arslan Salim Dar and Fernando Porté-Agel

Wind Engineering and Renewable Energy Laboratory (WIRE), École Polytechnique Fédérale de Lausanne (EPFL), 1015 Lausanne, Switzerland.

E-mail: arslan.dar@epfl.ch; fernando.porte-agel@epfl.ch

Abstract. Wind turbines are often sited on different topographical features. In the current work, we performed wind-tunnel measurements of the wake behind a single wind turbine sited on two escarpments differing in the windward side shape using tomographic particle-image velocimetry. The escarpments are classified as forward facing step (FFS) and ramp-shape. The turbine sited on the FFS experiences an inflow with high flow shear and turbulence due to flow separation from the escarpment leading edge compared to the one on the ramp-shaped escarpment. As a consequence, the wake characteristics behind the turbine are strongly affected by the shape of the topography. The velocity deficit in the wake of the turbine is relatively higher in the forward facing step shape, but it also shows a faster recovery. The rotation of the wake is stronger for the turbine on the ramp-shaped escarpment, whereas the meandering of the wake is higher for the FFS case. The spatial coherence is observed to be higher in the near wake of the turbine sited on the FFS escarpment, while it is very similar in the far wake for both cases. Instantaneous vortices identified by the Q-criterion show that the development of tip and hub vortices is affected by the topography as well.

Keywords: wakes, topography, tomographic particle-image velocimetry.

1. Introduction

Wind turbine wakes are characterized by highly complex three-dimensional flows due to the effects of boundary-layer flow shear, rotor rotation and multiple sources of vortex generation [1,2]. The development of these wakes is further dependent on different atmospheric conditions: thermal stratification, turbulence intensity and Coriolis force, to name a few [3–6]. In complex terrain, the presence of different topographical features further complicates the three-dimensional structure of wind turbine wakes. Understanding and quantifying these effects is, therefore, of great importance to predict wake effects in wind farms sited on topography [7, 8]. The information on the three-dimensional evolution of the wind turbine wakes can be useful for accurate estimation of the flow experienced by downstream wind turbines. This can facilitate the optimization of the turbine placement in a wind farm and provide basis for accurate power and load predictions. The most common laboratory measurement techniques, such as hot-wire anemometry, laser-doppler velocimetry and two-component or stereoscopic particle-image velocimetry (PIV), however, only provide point or planar measurements.

Tomographic particle-image velocimetry [9] is a powerful technique that enables instantaneous

flow measurements in a volume. The working principle behind the technique is briefly described in the following. The measurement volume filled with tracer particles is illuminated by a laser source. Multiple cameras are used to capture the light scattered by the particles from different angles. The numerical aperture of the cameras is increased in order to cover the depth of the measurement volume. A three-dimensional volume reconstruction is done from the acquired images using an iterative algebraic reconstruction technique. Finally, a three-dimensional cross-correlation is done on the reconstructed volume to obtain the velocity field. This technique has been proven useful to study three-dimensional flows, e.g., turbulent boundary layers [10] and trailing edge vortices [11]. The application of the technique for wind turbine wakes on topography is yet to be explored (to the best of the authors' knowledge).

In this study we attempt to characterize the three-dimensional flow field behind a single wind turbine sited on two different topographical features, namely, escarpments with a different windward side shape. The objective is to highlight the differences in the wake development that arise solely due to the change in the shape of the escarpment.

The rest of the article is outlined as follows. The experimental setup is presented in section 2. The two cases are analyzed in section 3. Finally, a summary of the work is given in section 4.

2. Experimental Setup

The experiments are performed in the boundary-layer wind tunnel at the WIRE laboratory of EPFL. The wind tunnel has a test section of $28 \times 2.56 \times 2\ m^3$, and a 130 kW fan drives the flow in the closed-loop tunnel. A contraction with a 5:1 area ratio is present at the inlet of the test section. Due to the length of the test section a natural boundary-layer develops over the surface without any tripping mechanism. A three-bladed horizontal axis wind turbine model [12] with a rotor diameter of 15 cm and hub height of 12.5 cm is placed one rotor diameter downstream from the leading edge of the escarpment. The turbine model is operated at a tip speed ratio $\lambda \approx 3.8$, which corresponds to the maximum power coefficient of the turbine.

Two topography models are used for the current study. The models are escarpments differing in the shape of the leading edge of the model. The length and width of the models is 3 m and 2.5 m respectively. The height is equal to the turbine hub height, i.e. 12.5 cm. One escarpment model is characterized by a sharp 90° edge (referred to as forward-facing step), whereas the second model has a sinusoidal ramp shape at the leading edge (referred to as ramp-shape). The ramp shape z_r is computed using the following equation:

$$z_r(x) = \frac{1}{2} H[1 + cos(\frac{\pi x}{2L})], \tag{1}$$

where H is the escarpment height and L is the half-length of the ramp, equal to 1.25 times the height, resulting in a maximum slope of about 33°. Figure 1 shows the side view of the escarpment model shapes.

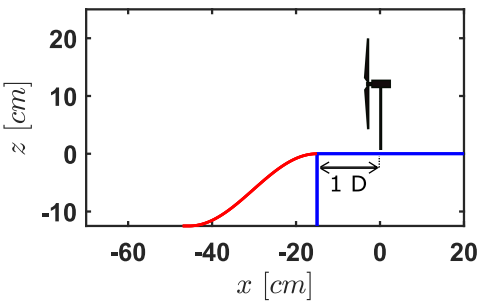

Figure 1. Side view of the topography leading edge. Blue: forward-facing step, and red: ramp-shaped escarpment.

The incoming velocity profile is characterized by a two-dimensional two-component (2D2C) PIV setup. The free stream velocity U_∞ is 4.37 ms^{-1}, whereas the velocity and streamwise

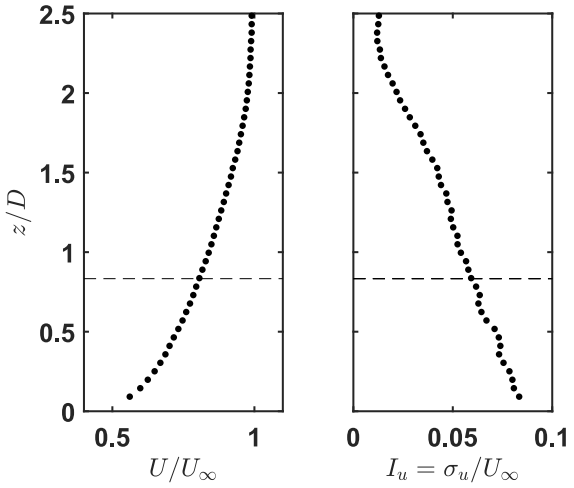

Figure 2. Vertical profiles of the normalized streamwise velocity (left) and streamwise turbulence intensity (right) in the upstream boundary-layer. The horizontal line indicates the projected topography height.

turbulence intensity at the escarpment height are 3.55 ms^{-1} and 6% respectively. Figure 2 shows the incoming velocity and streamwise turbulence intensity profiles. The boundary layer thickness is 39 cm, and the roughness length and friction velocity are computed to be 0.04 mm and 0.17 ms^{-1} respectively.

2.1. Tomographic particle-image velocimetry

A tomographic particle-image velocimetry system is used to measure the flow in a volume of $2D \times 2D \times 1.5D$ ($x \times y \times z$) at a spatial resolution of $0.023D$, where D is the rotor diameter. The camera setup consists of four 16-bit sCMOS cameras (2560 $\times$ 2160 pixels), mounted on Scheimpflug adapters with 55 mm objectives. To cover the depth of focus of the target volume, the aperture of the objectives is set to $f/16$ (with f being the focal length), and the center of the focal depth is aligned with the center of the illuminated volume. A double-pulse 435 mJ Nd:YAG laser is used as the laser source, and a combination of converging and diverging lenses is used to expand the laser beam into a volume. A helium-filled soap bubble generator system developed by LaVision is used to generate neutrally buoyant soap particles with a diameter on the order of 1 mm. The soap bubbles produced this way are much brighter compared to the conventional oil/aerosol particle seeding methods and facilitate PIV measurements at low light intensity. The bubbles are injected into the flow using a fluid supply unit at approximately 15 m upstream of the measurement volume. Figure 3 shows a schematic representation of the tomo-PIV setup.

A target calibration using a 3D calibration plate developed by LaVision is initially conducted, where images at five equidistant planes within the target volume are used. Following the physical calibration, images are acquired at a sampling rate of 10 Hz and a total of 1000 image pairs are used to obtain the ensemble averaged flow field. The captured images are pre-processed by subtracting a sliding minimum over each 3 pixels, normalizing with a local average over 50 pixels and, finally, performing a Gaussian smoothing over a 3×3 pixel window. The physical calibration is further improved by a self-calibration method [13], following which the volume reconstruction is done. A multiplicative algebraic reconstruction technique (MART) [14] is used for this purpose. For the current study, we perform six MART iterations for each volume reconstruction. The quality of the reconstructed volume is ensured by maintaining the signal-to-noise ratio above 5. The reconstructed field is then used for volume correlation, which is done in three decreasing interrogation volumes from $96 \times 96 \times 96$ voxels to $64 \times 64 \times 64$ voxels to $48 \times 48 \times 48$ voxels. Each interrogation volume has 75% overlap and the correlation is obtained after two passes through each volume. A total of three fields of view are obtained for each case,

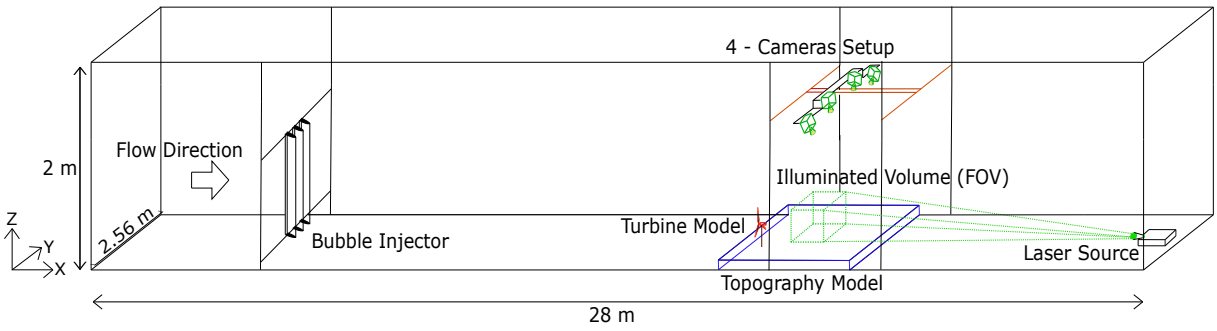

Figure 3. Schematic representation of the tomographic PIV setup.

and an overlap of approximately 10% is kept between different fields of view.

3. Results

3.1. Mean flow characteristics

We first focus on the mean characteristics of the wake behind the turbine. Figure 4 shows the normalized mean streamwise component of the flow velocity for the two cases. The hub height streamwise velocity at the turbine location without the turbine U_h is chosen for normalization in respective cases throughout the article. Using isosurfaces, we isolate different features of the wake flow. In the case of the turbine on the FFS escarpment, the wake appears to be stronger and has a higher expansion rate compared to the one on the ramp-shaped escarpment. A downward shift in the wake position is also observed as it moves downstream. The shape of the wake is relatively more asymmetric for the turbine on the FFS escarpment than for the one on the ramp-shaped escarpment. This is because the shear induced by the FFS escarpment is higher than that induced by the ramp-shaped escarpment.

While the streamwise velocity component shows the combination of the wake and the ambient flow, the streamwise velocity deficit, computed as $\Delta U = U_{nw} - U_w$, is used to determine the

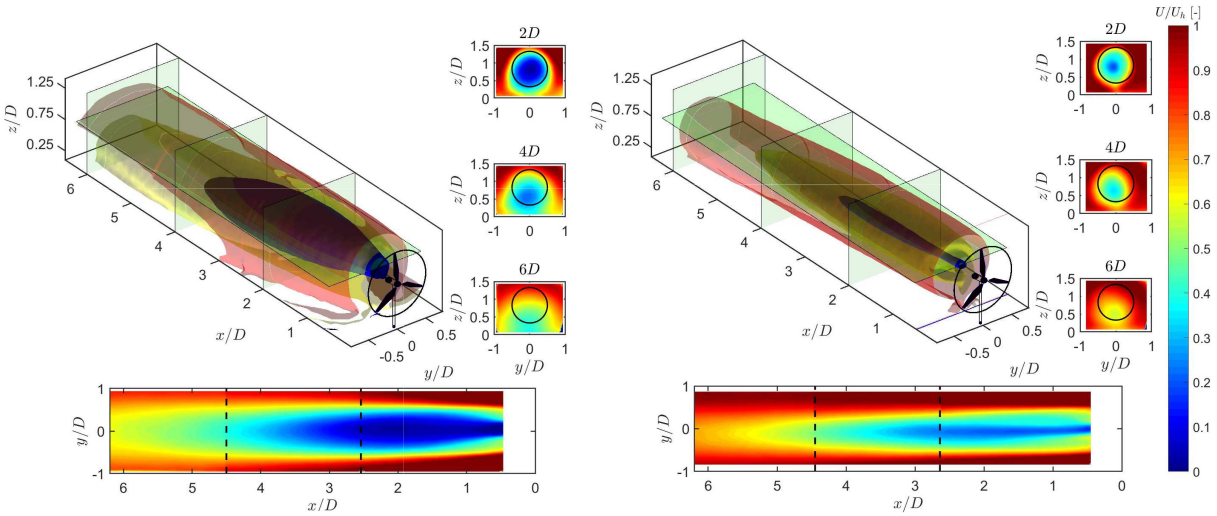

Figure 4. Normalized mean streamwise velocity component for the turbine sited on forward facing step (left) and ramp-shaped (right) escarpments. Isosurfaces correspond to: U/U_h=0.75 (red), U/U_h=0.5 (yellow) and U/U_h=0.25 (blue). Contour plots correspond to information extracted from highlighted planes in the three-dimensional plot.

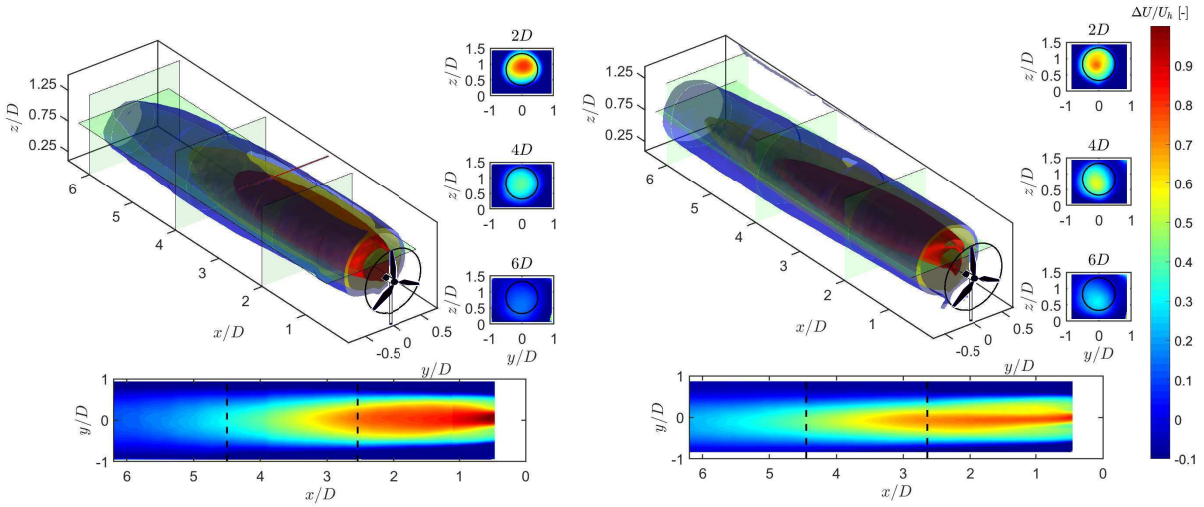

Figure 5. Normalized mean streamwise velocity deficit for the turbine sited on forward facing step (left) and ramp-shaped (right) escarpments. Isosurfaces correspond to: $\Delta U/U_h$=0.5 (red), $\Delta U/U_h$=0.3 (yellow) and $\Delta U/U_h$=0.1 (blue). Contour plots correspond to information extracted from highlighted planes in the three-dimensional plot.

effect of the turbine on the flow. Here, U_{nw} is the velocity without the turbine and U_w is the velocity in the presence of the turbine. In the current study, U_{nw} is obtained from stereoscopic PIV measurements and figure 5 shows the velocity deficit for the two cases. The isosurface corresponding to $\Delta U/U_h = 0.5$ encloses the region with high velocity deficit and is observed to be wider for the FFS case. This isosurface allows to identify the downstream location where the wake is recovered by 50%, which is around 3.65D and 4.35D for the turbine on the FFS and ramp-shaped escarpment, respectively. The location where the wake is recovered by 70% is shown by the yellow isosurface ($\Delta U/U_h = 0.3$), which also happens earlier for the turbine on the FFS compared to the one on the ramp-shaped escarpment. The blue isosurface ($\Delta U/U_h = 0.1$) shows the size of the wake itself, and is observed to be bigger for the FFS case. In general, the velocity deficit is comparatively higher for the turbine on the FFS escarpment, but it also exhibits a faster rate of recovery.

The information gained from the three-dimensional development of the streamwise velocity can be used to estimate the power available for an in-wake turbine. To compare the power available in the wake of the turbine we use the following expression by Vollmer et al. [15]:

$$f_{AP} = \frac{1}{2}\rho \int_{y_1}^{y_2} \int_{z_1}^{z_2} U^3(y,z) dz dy, \tag{2}$$

where $y^2 + (z - z_h)^2 \leq (D/2)^2$ and z_h is the hub height of the turbine. The computed available power is then normalized by the reference $f_{AP,ref} = 1/2\rho A U_h^3$. Figure 6 shows a comparison of the normalized available power for the two escarpment cases. As can be seen, the available power is higher in the wake of the turbine sited on the ramp-shaped escarpment than in that on the FFS escarpment. For instance, at a downstream distance of 5 rotor diameters, the f_{AP} is almost double for the ramp-shaped escarpment case than for the FFS case. This indicates that a potential wind farm sited on the ramp-shaped escarpment could have a better power performance compared to a wind farm sited on the forward facing step escarpment.

We now compare the strength of the wake rotation in the two cases. Figure 7 shows the streamlines tracking mean flow from different initial points, overlaid by the in-plane velocity vectors at different planes parallel to the rotor plane. Comparing the two cases, the wake

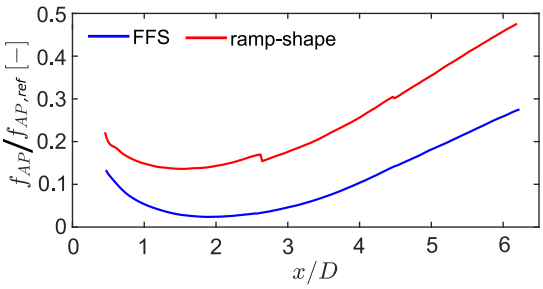

Figure 6. Comparison of the normalized available power in the turbine wake for the two escarpment cases.

rotation is relatively stronger for the turbine sited on the ramp-shaped escarpment. It also lasts a longer distance for the turbine on the ramp-shaped escarpment than for the one on the FFS escarpment. The relatively weaker rotation of the wake behind the turbine sited on the FFS escarpment can be associated with higher turbulence in the inflow originating from the separated flow from the leading edge of the escarpment. In the far wake, the entrainment of outer flow into the wake can be observed around the rotor top, which plays a role in the recovery of the wake. In order to understand the trajectory of the wake, the streamlines tracking the mean flow are discussed here. We first look at the streamlines numbered 1-4 in figure 7 side panels. The streamlines 1,2 originate around the bottom left of the rotor and the streamlines 3,4 initiate from the upper right part of the wake. These streamlines show a higher deflection from the wake center with the increase in downstream distance for the turbine on the FFS escarpment compared to the one on the ramp-shaped escarpment. This can be associated with the size of the wake observed in figure 4 and indicates that the wake has a comparatively higher expansion rate in the FFS case. Another important observation is the downward trajectory of the streamlines, showing a downward motion of the wake with downstream distance. This downward motion is higher for the turbine on the FFS escarpment, which shows that the wake gets more attached to the surface in this case compared to the case of the ramp-shaped escarpment.

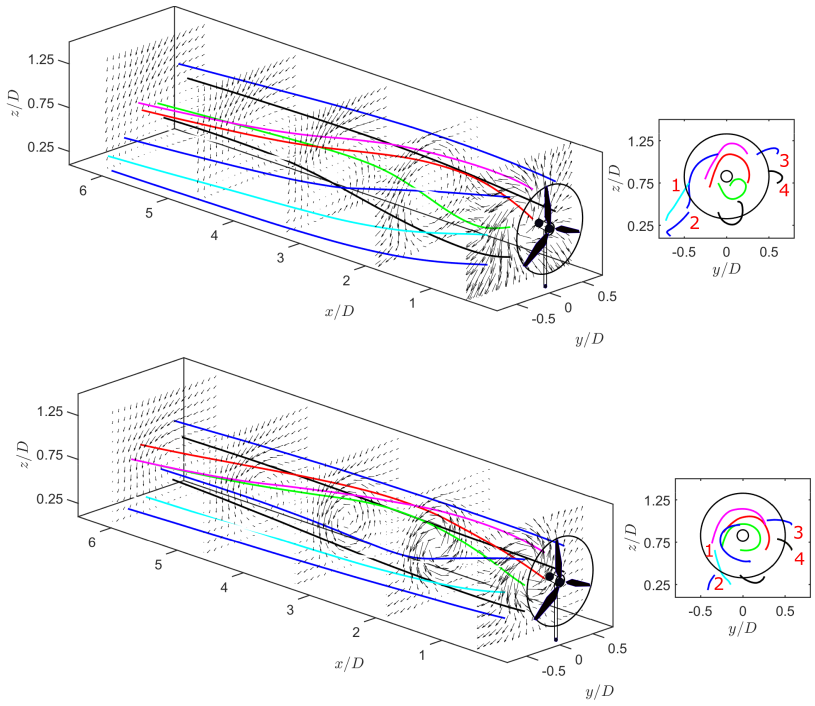

Figure 7. Streamlines tracking the mean flow trajectory in the wake of the turbine sited on forward facing step (top) and ramp-shaped (bottom) escarpments. In-plane velocity vectors are displayed at selected planes parallel to the rotor plane. Side panels show the front view of the three-dimensional plot.

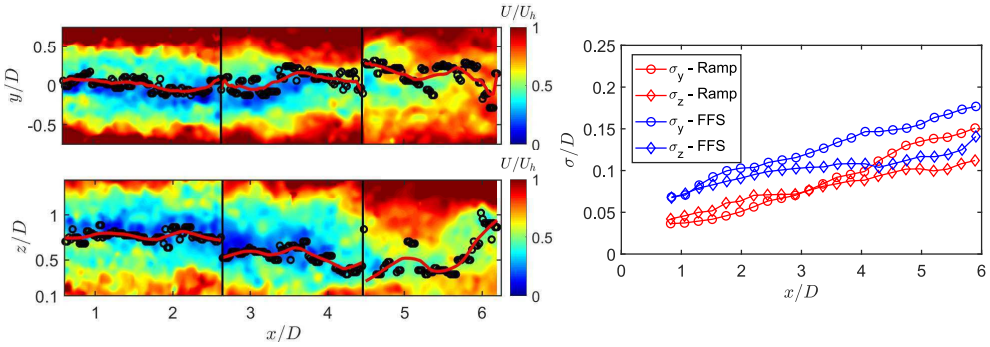

Figure 8. Left panel: instantaneous streamwise velocity contours in the lateral and vertical planes passing through the turbine hub and centerline, respectively, for the ramp-shaped escarpment case. The projections of the three-dimensional distribution of the streamwise velocity minimum and spatially filtered meandering profile on two-dimensional planes are represented by black circles and red line, respectively. Different fields of view are separated by the black vertical lines. Right panel: normalized standard deviation of the Gaussian fit to the spatially filtered instantaneous streamwise velocity minimum as a function of the downstream distance.

3.2. Dynamic characteristics

The difference in the ambient flow conditions the turbine is exposed to in the two escarpment cases has an effect on the dynamic wake characteristics. Herein this section we study the wake meandering, flow coherence and vortical structures from the tomo-PIV measurements.

Meandering is an important dynamic characteristic due to its implications for the fluctuating loads on the downwind turbines. Here, we characterize the magnitude of the meandering motions using the three-dimensional distribution of the instantaneous streamwise velocity minimum [16]. To obtain a smooth meandering profile, a spatial moving average filter with a window length of 0.5D is applied on the instantaneous streamwise velocity minimum. The size of the window length is chosen such as to remove the effect of the small scale velocity fluctuations, meanwhile maintaining the coherent structure of the meandering motion. An example of the obtained meander profile in three separate time instants (one for each field of view) for the turbine on the ramp-shaped escarpment is shown in figure 8 (left panel).

Figure 9 shows the distribution of the spatially filtered instantaneous streamwise velocity minimum for the two escarpment cases. The magnitude of meandering is observed to increase with the downstream distance, and the instantaneous velocity minimum distribution shows a downward trajectory for both cases. To characterize the increase in meandering with the

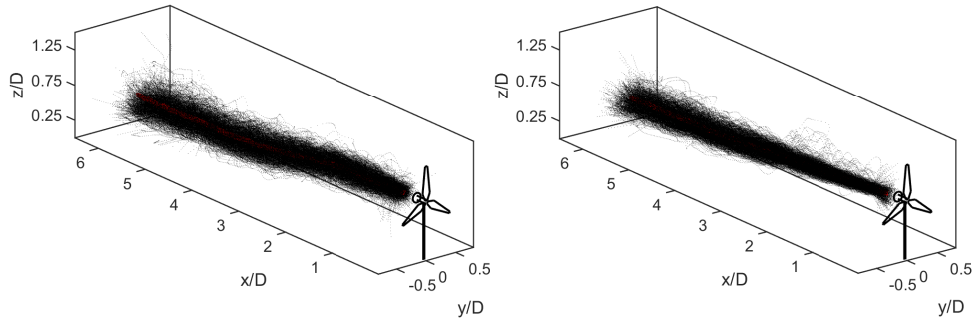

Figure 9. Three-dimensional distribution of the spatially filtered instantaneous streamwise velocity minimum for the turbine sited on the forward facing step (left) and ramp-shaped (right) escarpments.

downstream distance, we plot the normalized standard deviation of the Gaussian fit to the lateral and vertical instantaneous streamwise velocity minimum distribution in figure 8 (right panel). In the near wake, the lateral and vertical standard deviations are very close to each other for the respective cases. The difference in these standard deviations, however, increases with the increase in downstream distance with the lateral standard deviation showing higher values than the vertical one. Comparing the two escarpment cases, the turbine on the FFS escarpment shows higher standard deviation values, both in the vertical and lateral direction than the turbine on the ramp-shaped escarpment. This shows that the meandering of the turbine wake is higher when it is sited on the FFS escarpment than when it is sited on the ramp-shaped escarpment. This can be related to the higher turbulence and unsteadiness in the incoming flow for the turbine on the FFS than for the one on the ramp-shaped escarpment.

The spatial coherence of the streamwise velocity fluctuations is investigated using two-point spatial correlation in a three-dimensional space. The spatial correlation is computed for the streamwise velocity fluctuation component as follows:

$$R_{uu} = \frac{\overline{u'(x_{ref}, y_{ref}, z_{ref}) u'(x, y, z)}}{\sqrt{\overline{u'(x_{ref}, y_{ref}, z_{ref})^2} \times \overline{u'(x, y, z)^2}}}, \tag{3}$$

where $u'(x_{ref}, y_{ref}, z_{ref})$ is the reference indicated by black points in the isosurface plots shown in figure 10. In general, the spatial coherence is small for the region closest to the turbine and it increases with increasing downstream distance. In the near wake region of the two cases, the spatial coherence is observed to be higher for the turbine on the forward facing step escarpment, whereas in the far wake it is similar for both cases. As discussed by Bastankhah & Porté-Agel [17], the spatial coherence in the near wake is influenced by the shear layer developed around the turbine nacelle. The small coherence observed in the near-wake of the turbine on the ramp-shaped escarpment is found to be consistent with the fact that the shear layer developed around the turbine nacelle is stronger in this case compared to the one of the turbine on the FFS (see figure 11).

Vortices generated by the rotor blades and the hub are an important dynamic characteristic of the turbine wake. To identify vortices in the instantaneous three-dimensional field we use Q-criterion, which quantifies the relative amplitude of the rotation rate and strain rate, revealing

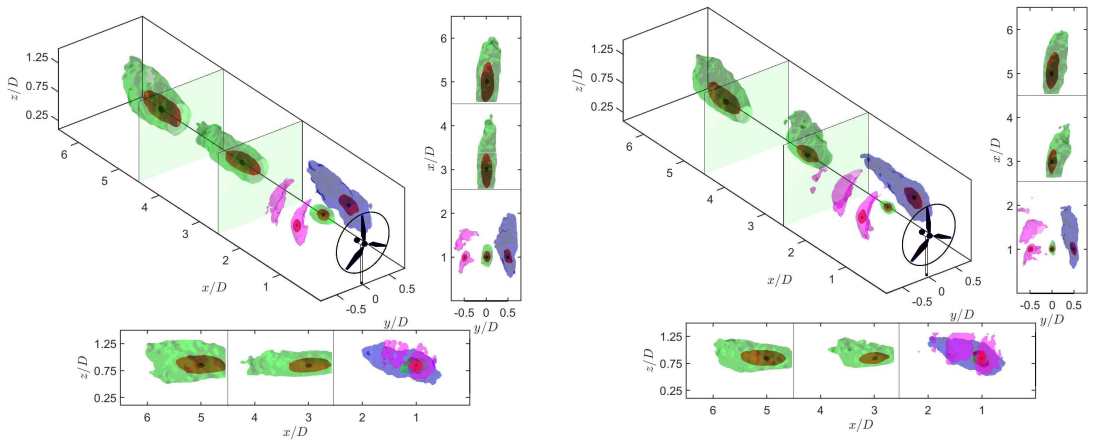

Figure 10. Two-point spatial correlation of the streamwise velocity fluctuations at different spatial locations for the turbine sited on the forward facing step (left) and ramp-shaped (right) escarpments. The isosurfaces correspond to $R_{uu} = 0.95$ (black) (location of the reference point), $R_{uu} = 0.5$ (red) and $R_{uu} = 0.25$ (green, magenta, purple). Green planes separate consecutive fields of view.

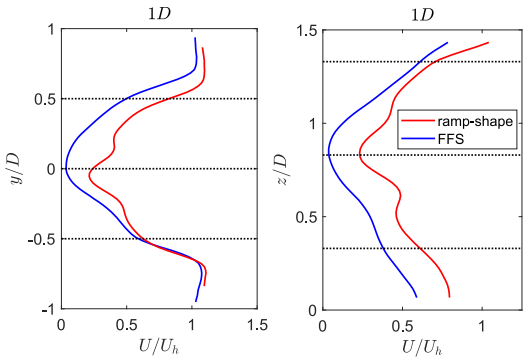

Figure 11. Lateral (left) and vertical (right) profiles of the normalized mean streamwise velocity component at a downstream distance of 1 rotor diameter. The horizontal black lines show rotor tips and hub locations.

the vortex cores. The Q-criterion is computed as follows:

$$Q = \frac{1}{2}(||\Omega_{ij}||^2 - ||S_{ij}||^2), \tag{4}$$

where $\Omega_{ij} = \frac{1}{2}(\frac{\partial u_i}{\partial x_j} - \frac{\partial u_j}{\partial x_i})$ is the vorticity tensor, $S_{ij} = \frac{1}{2}(\frac{\partial u_i}{\partial x_j} + \frac{\partial u_j}{\partial x_i})$ is the strain rate tensor and $||.||$ represents the Euclidean norm [18]. Figure 12 shows the isosurface plots of the normalized instantaneous Q-criterion for the two cases, colored by the normalized instantaneous streamwise velocity. Individual spirals from the tip vortices can be identified in the near wake of the two cases. The helical shape of the tip vortices lasts up to a downstream distance of about 2 times the rotor diameter for the turbine on the FFS, beyond which breakdown of tip vortices happens. For the case of the turbine on the ramp-shaped escarpment, these tip vortices last up to 2.5D. The strength of the tip vortices is also higher for the turbine on the ramp-shaped escarpment compared to the one on the FFS. The weaker strength and earlier breakdown of the tip vortices in the FFS case can be associated with the relatively higher turbulence in the inflow compared to the case of the ramp-shape. Another important observation is the hub vortex, which is broken in the forward facing step case but is still intact in the near wake of the turbine on the ramp-shaped escarpment. The broken hub vortex in the FFS case can be seen hitting the tip vortices, which also plays a role in the reduced strength and breakdown of the tip vortices in this case.

4. Conclusions

Experimental observations of complex three-dimensional flows in a volume are a powerful tool to understand the spatial development of such flows. In the current work, we performed

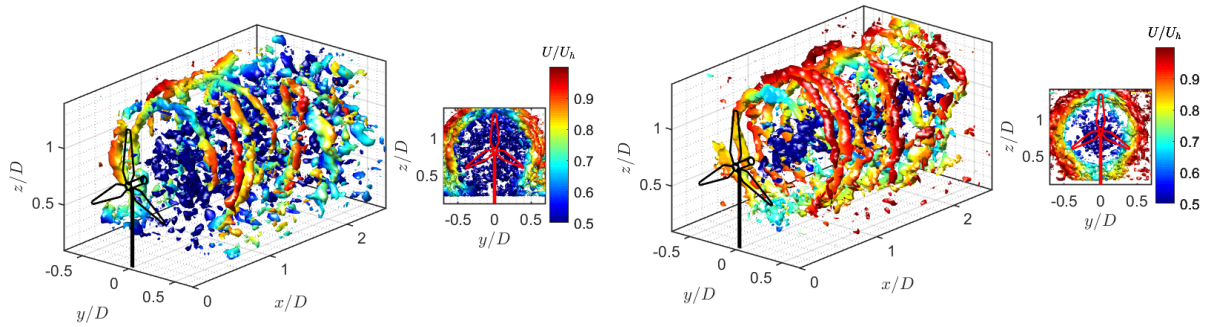

Figure 12. Isosurfaces of the normalized instantaneous Q-criterion ($QD^2/U_h^2 = 5$) for the turbine sited on the forward facing step (left) and ramp-shaped (right) escarpments. The isosurfaces are colored by the instantaneous normalized streamwise velocity. Side panels show the front view of the three-dimensional plot.

tomographic particle-image velocimetry for a single turbine wake sited on two different topographical features: a forward facing step and a ramp-shaped escarpment. The two topographies induced different levels of flow shear and turbulence which eventually had a strong influence on the wake characteristics of the turbine sited on them. Focusing on mean flow characteristics, we highlighted key differences in the development of the turbine wake caused primarily by the difference in the shape of the topography. The wake showed a higher velocity deficit for the turbine on the forward facing step escarpment, but also recovered quicker compared to the one on the ramp-shaped escarpment. The rotation of the wake was found to be comparatively stronger for the turbine on the ramp-shaped escarpment. Extending the analysis to the dynamic wake characteristics, the wake meandering was observed to be stronger for the turbine wake on the FFS escarpment due to higher turbulence in the inflow and unsteady nature of the flow separation from the leading edge of the escarpment. The spatial coherence was higher in the near wake of the turbine on the FFS escarpment which was associated with the shear in the flow, however it was similar in the far wake for both cases. Finally, we studied vortex shedding from the rotor tips and hub. The tip vortices shed by the turbine on the ramp-shaped escarpment lasted longer distance than by the turbine on the FFS escarpment. The hub vortex in the near wake was broken in the FFS case, whereas it was intact in the ramp-shaped escarpment case.

Funding
This research was funded by the Swiss National Science Foundation (grant number: 200021_172538) and the Swiss Federal Office of Energy. In addition, this project was carried out within the frame of the Swiss Centre for Competence in Energy Research on the Future Swiss Electrical Infrastructure (SCCER-FURIES) with the financial support of the Swiss Innovation Agency (Innosuisse - SCCER programme, contract number: 1155002544).

Acknowledgments
The authors would like to thank Haohua Zong for assistance in preparation of the experimental setup.

References
[1] Vermeer L J, Sørensen J N and Crespo A 2003 *Progress in aerospace sciences* **39** 467-510.
[2] Zhang W, Markfort C D and Porté-Agel F 2012 *Experiments in fluids* **52** 1219-1235.
[3] Chamorro L P and Porté-Agel F 2010 *Boundary-layer meteorol.* **136** 515-533.
[4] Bhaganagar K and Debnath M 2014 *Energies* **7** 5740-5763.
[5] Vollmer L, Steinfeld G, Heinemann D and Kühn M 2016 *Wind Energ. Sci* **1** 129-141.
[6] Abkar M and Porté-Agel F 2016 *Physical Review Fluids* **1** 063701.
[7] Porté-Agel F, Bastankhah M and Shamsoddin S 2020 *Boundary-Layer Meteorol.* **174** 1-59.
[8] Fernando H J S, et al. 2019 *Bulletin of the American Meteorological Society* **100** 799-819.
[9] Elsinga G E, Scarano F, Wieneke B and van Oudheusden B W 2006 *Experiments in fluids* **41** 933-947.
[10] Elsinga G, Kuik D J, Van Oudheusden B and Scarano F 2007 *45th AIAA aerospace sciences meeting and exhibit* p 1305.
[11] Ghaemi S and Scarano F 2011 *Journal of Fluid Mechanics* **689** 317-356.
[12] Bastankhah M and Porté-Agel F 2017 *Energies* **10** 908.
[13] Wieneke B 2008 *Experiments in fluids* **45** 549-556.
[14] Herman G T and Lent A 1976 *Comput. Biol. Med.* **6** 273-294.
[15] Vollmer L, Steinfeld G, Heinemann D and Kühn M 2016 *Wind Energ. Sci.* **1** 129-141.
[16] Howard K B, Singh A, Sotiropoulos F and Guala M 2015 *Physics of Fluids* **27** 075103.
[17] Bastankhah M and Porté-Agel F 2017 *Physics of Fluids* **29** 065105.
[18] Haller G 2005 *Journal of Fluid Mechanics* **525** 1-26.